Study of Adsorption of Orange G and Malachite Green on the Surface of Znfe2o4-PANI Nanocomposite Prepared by in-Situ Polymerization Method

Zain Al-Abidine Naji Al-Hasnawy[1], Khawla Kani Jasim[2], and Masar Ali Awad[3]
[1, 2,3]Department of Chemistry, College of Science, Al-Muthanna University, Iraq
Corresponding Authors
Zain Al-Abidine Naji Al-Hasnawy
zeinalabdeen.naji.scih@mu.edu.iq, khawla.kani@mu.edu.iq, masara32@yahoo.com

Abstract

ZnFe2O4 Nanoparticles were synthesized using a Co-precipitation method and impregnating ZnFe2O4 Nanoparticles onto polyaniline (PANI) by in-situ polymerization under ultrasonic fields. Used X-ray diffraction (XRD), Field Emission Scanning Electron Microscope (FE-SEM), Vibrating-Sample Magnetometer (VSM), Surface area analysis (BET, BJH), Fourier Transform Infrared Spectroscopy (FT-IR), Atomic Force Microscope (AFM), and Thermal Gravimetric Analysis (TGA) were used to characterize the magnetic nanocomposite of (PANI-ZnFe2O4). The FTIR Spectroscopy exhibits the emergence and shifts in the main bands and average crystal sizes of nanocomposite materials (26.39 nm) for PANI-ZnFe2O4 are different from ZnFe2O4. Additionally, The ZnFe2O4 Nanoparticles are homogeneously dispersed throughout the PANI matrix, according to the AFM and FE-SEM images. The thermodynamic study concluded that the adsorption of both dyes was spontaneous in nature and exothermic. The adsorption pursued pseudo-second-order kinetics. In addition, the isotherm models Freundlich, Langmuir, and Timken were used to model the experimental adsorption data. To match the experimental isotherm, the Langmuir isotherm was employed.

Graphical abstract

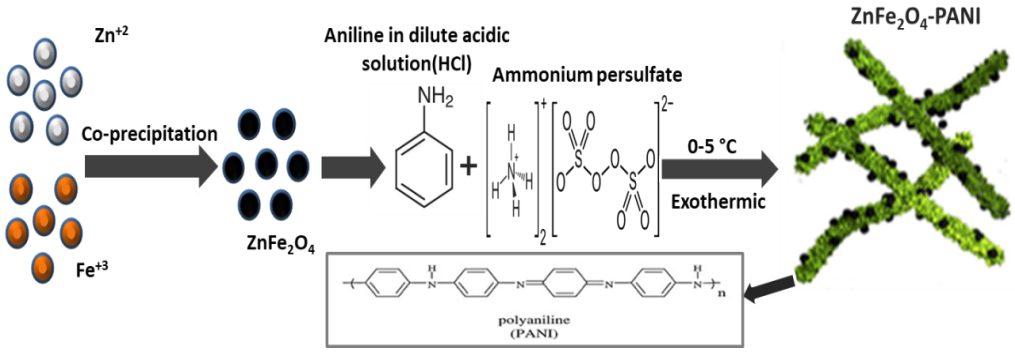

Keywords: Nanocomposite, Spinel Ferrite, PANI, Adsorption, Water treatment

1. Introduction

Pollutants are one of the most important issues facing the world. Pollution has risen significantly in recent years, reaching frightening levels in terms of its effects on living things [1]. Environmental contaminants have been generated as a result of increased demand for rapid urbanization and shifting consumer habits, as well as unrestricted population expansion, rapid socioeconomic development, and changes in energy sources, medicine, agriculture, and chemical industries. These pollutants are released into the atmosphere, water, and soil, causing harm to humans, plants, animals, and microbes [2]. Colored effluents from a variety of industries, including textiles, cosmetics, paper, laundry, leather, printing, food and beverage, pharmaceuticals, and carpet, are extremely toxic and pose a significant threat to aquatic ecology, and human health [3]. Around 10,000 types of synthetic and natural dyes are generated annually around the world, weighing roughly 7105-1106 tonnes, and a large proportion of dye is wasted during industrialization [4]. In addition, during the textile coloring process, a large number of chemicals and dyestuffs go wasted, and the excess dye liquid is released into the environment. Due to its low adsorption capacity, it is estimated that the dyed textile material may absorb roughly 80% of the dyes and compounds from the dye liquor [5].

To reduce the environmental impact of synthetic dyes, a variety of methods for removing them from water and wastewater have been developed. Adsorption is a well-known method around the world. Water purification using low-cost adsorbents is a practical method. Besides, adsorption has an advantage over other methods since it is a sludge-free, clean method that removes dyes fully even from diluted solutions [6]. Because of their high surface to volume ratio, superparamagnetic

doi.org/10.31838/hiv22.02.271 Received: 16.06.22, Revised: 17.07.22, Accepted: 06.08.22

characteristics, and nanoscale size, a wide range of nanomaterials, including ferrite spinels, are being employed for a variety of applications such as water and wastewater treatment. Because agglomeration is a major issue with nanomaterials, polymer nanocomposites are widely utilized as adsorbents for dye removal. Polymer systems are inherently non-magnetic, but the impregnation of magnetic ferrite into the polymer matrix adds magnetic characteristics and significantly improves physical qualities [7]. As a result, PANI is commonly used to remove dyes from pollutant wastewater.

2. Materials and Methods

Materials

All chemicals and reagents, including aniline (which was distilled before it was used), hydrochloric acid (HCl), ferric chloride (FeCl3), zinc chloride (ZnCl2), ammonium hydroxide solution (NH4OH), ammonium peroxodisulphate ((NH4)2S2O8), orange G (OG) dye with following information (molecular weight: 452.4 g/mol, empirical formula: C16H10N2Na2O7S2), malachite green (MG) dye with following information (molecular weight: 364.911 g/mol, empirical formula: C23H25ClN2) were obtained from Sigma-Aldrich (USA).

Preparation of Zinc Ferrite ($ZnFe_2O_4$) nanoparticles

Spinel ferrite ZnFe2O4 was synthesized by the method of Co-precipitation. Firstly FeCl3 (6.49 g, 0.04 mol) solution was mixed with ZnCl2 (2.726 g, 0.02 mol) solution under vigorous stirrer for 25 min at 70oC. Secondly, ammonium solution (2M) was dropped wise to the mixture under ultrasound waves (energy 350 w, 40 kHz) until reached PH (10) and formed a brown colloidal solution. The brown precipitate was separated by centrifuge, then washed several times with hot water. Finally, ZnFe2O4 precipitate was dried by oven at 80oC overnight and then dried ZnFe2O4 calcinated at 600 °C for 3hrs [8].

Preparation of PANI-ZnFe2O4 nanocomposite

Preparation of the PANI-ZnFe2O4 nanocomposite with a ratio of (9:1) by in situ oxidative polymerization. Firstly, (0.113) g of Zinc ferrite and (1) ml of aniline monomer are added to (100) ml of (0.11) M HCl solution under ultrasound waves (energy 350w, 40 kHz) for 30 min to obtain a homogeneous dispersion. Secondly, the prepared mixture is placed ice bath under ultrasound waves and added (2.51) g ammonium persulfate solution was dropped wise for 1 hr. After that, mixture is left until the polymerization process is completed for 24 hrs. Finally, the sample washing with distilled water until the nominate was colorless and then was dried for 24 hrs in the oven at 50 °C [9].

Characterization of PANI-$ZnFe_2O_4$ nanocomposite

FTIR with a wavenumber range of 400–4000 cm-1 (Shimadzu, Japan, FTIR 8400s) spectra to ZF nanoparticles, PANI, and ZF-PANI nanocomposites were used to determine the functional groups. The UV–Visible Spectrophotometer (UV-1800 PC Shimadzu) was used to measure the spectrum in the range of (200–800) nm. The morphology of ZF nanoparticles, PANI, and ZF-PANI nanocomposites was studied using a field emission scanning electron microscope (Fesem Tescan Mira3, France) with a 15 kV accelerating voltage, and the roughness of the nanocomposites' surface was measured using an angstrom AFM (SPM-AA3000, USA). The crystalline phase of samples was characterized by XRD using (BrukerAXSGmbh, Germany/D2 Phaser) with CuKα radiation (0.15040nm) and the XRD pattern was recorded ranging from 5 to 90°. The surface area and porosity analysis of ZF-PANI nanocomposite were obtained with Quantachrome Instruments (Nova 2200e, USA) and methods the multipoint of (BET) and (BJH). Vibrating-sample magnetometer (VSM-7300, Lake Shore) was used to measure the saturation magnetization, and under nitrogen atmosphere, the curve of thermogravimetric analysis (TGA) was done by Perkin Elmer (TGA 4000).

Adsorption experiments

Batch adsorption

The adsorption tests of OG and MG by using ZnFe2O4/PANI composites were used according to the batch experiments to determine adsorption parameters such as contact time initial dye concentration, temperature, initial pH solution, and adsorbent dose by altering one parameter at a time while the other parameters are fixed. After preparing 1000 ppm stock solutions of OG or MG, the batch adsorption solutions were prepared by diluting the stock solution. The experiments were carried out in a cylindrical glass with an equivalent capacity (10 ml aqueous samples), with specified adsorbents added at known initial concentrations of OG or MG. To test the effect of solution pH, specific volumes of distilled water with a specific pH (adjusted with dilute HCl or NaOH) were added to the OG and MG solutions. The solutions were vigorously stirred at 120 rpm on a shaker water bath for the required time of equilibrium. After separating the suspended substance, the equilibrium concentration of the solution was determined using UV-Visible spectroscopy at λ max nm. Equations 1 and 2 were used to calculate the quantity and removal percentage respectively of adsorbed dye on adsorbent at the equilibrium time (qe).

$$q_e = \frac{V\,(C_0 - C_e)}{m} \quad (1)$$

$$Removal(\%) = \frac{C_0 - C_e}{C_0} \times 100 \quad (2)$$

Where C_0 and C_e are the initial and final concentrations (mg/L) of OG and MG dye in an aqueous solution, respectively. q_e (Mg g-1), is the amount of OG and MG adsorbed on fixed adsorbent mass (g) at the time of equilibrium. V is volume (in L) of the initial OG and MG solution.

3. Results and Discussion

Characterization

Functional groups

The existence of functional groups and the nature of molecular bonds in the material can be determined using FT-IR. The FT-IR spectrum of ZnFe2O4 nanoparticles,

PANI, and ZnFe2O4-PANI nanocomposite were shown in Fig. 1. ZnFe2O4 spectrum shows two characteristic peaks; the first peak assigned to the vibrational bond at 553 cm-1 which relates to the metal at the tetrahedral site (Zn-O) possessing inherent stretching vibrations, whilst the second is assigned to the vibrational bond at 430 cm-1 corresponds to the octahedral metal stretching vibration (Fe-O) [10]. For PANI spectrum shows the following peaks: The band at 3217.37 cm-1 and 3205.80 cm-1 represents the N–H stretching vibration. The stretching vibration of C=C in an asymmetrical benzene ring, corresponding to the structure of quinoid (N=Q=N) and benzene (N–B–N), is assigned at 1572.04 and 1496.81 cm-1, respectively. The stretching vibration of C–N is responsible for the two peaks positioned at 1301.99 and 1247.99 cm-1. The prominent peak at 1126.47 cm-1 corresponds to the in-plane bending vibration of C–H generated by protonation, which is the distinctive absorption of PANI. At 505.37 cm-1(assigned to the aromatic ring of bonding mode C–N–C), the two peaks 605.67 cm-1 and 690.59 cm-1 (assigned to the aromatic ring of bonding mode C–C, C–H), while the peak 813.99 cm-1(assigned to the out-of-plane bending vibration of C–H) and are the characteristic absorption bands of PANI also [11]. As shown from Fig. 1, all peaks of PANI and ZnFe2O4 nanoparticles are representative in the FTIR spectrum of prepared nanocomposite; In addition, a band of 3205 cm–1 was shifted to higher wavenumber of 3435 cm–1 due to the weakness of the PANI intermolecular hydrogen bonding between its molecules after composition with ZnFe2O4 [12].

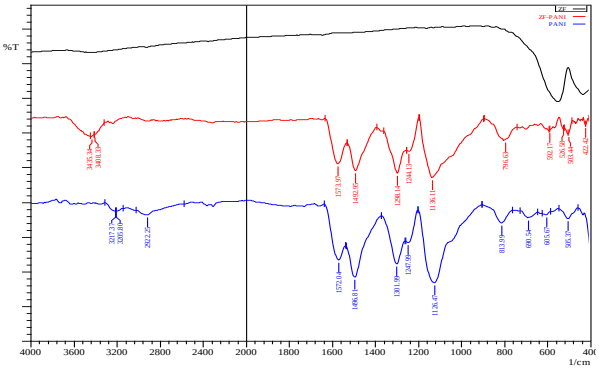

Fig. 1. FTIR spectra of $ZnFe_2O_4$ nanoparticles, PANI, and prepared nanocomposites.

Crystalline structure

The crystalline structure of ZnFe2O4 and prepared nanocomposite were examined the X-ray diffraction technique, Fig. 2 shows the XRD patterns of ZnFe2O4 nanoparticles, PANI, and prepared nanocomposite ZnFe2O4-PANI. Four characteristic peaks of PANI can be found at 2θ = 8.7, 15.4, 20.2, and 25.98, where The XRD pattern shows a broad diffraction peak at 15.4 and 20.2 with one weak peak at 8.7, indicating that the PANI molecular chain is amorphous, while the diffraction peak at 25.98 suggests that the PANI molecular chain has a degree of crystallinity, which could be due to doping with HCl. The crystallization behavior of the PANI molecular chain is hampered by the hardness of the benzene ring, therefore the latter peak is not highly sharp [11, 13]. Whilst the ZnFe2O4 nanoparticles pattern exhibits diffraction peaks that are well indexed to purely cubic phase according to phase matches well with the standard JCPDS card No. 22-1012 [11]. The diffracted crystal planes of ZnFe2O4-PANI nanocomposite were matched using the XRD patterns of ZnFe2O4 and PANI, which exhibited a combination of both diffraction peaks acquired from pure PANI and ZnFe2O4, ensuring the nanocomposite's formation. During the polymerization process, the crystal structure of ZnFe2O4 is partially distorted [9].

According to Scherrer's equation (eq.3) [9], the average crystal size of nanocomposite materials was calculated and placed in a table (1).

$$D = \frac{k\lambda}{\beta \cos\theta} \quad (3)$$

Where: k: is the shape factor which usually takes a value of about (0.94), λ is the incident x-ray wavelength (0.15040 nm for CuK) , β is full width at half maximum (FWHM), and θ is diffraction angle at maximum intensity peak.

Table (1): Represent the average crystal sizes of ZnFe2O4 and its nanocomposite.

NO.	prepared materials	Peak Position (2θ)	FWHM (2θ)	average crystal sizes (nm)
1	ZnFe2O4	35.3141	0.2362	36.88
2	ZnFe2O4/PANI	35.257	0.3300	26.39

From the table, we see that the average crystal sizes of nanocomposite materials for ZnFe2O4/PANI are different from ZnFe2O4 which is lead to getting on a good mixing of Nanocomposite that was clearly in Fig.(4) for FE-SEM images.

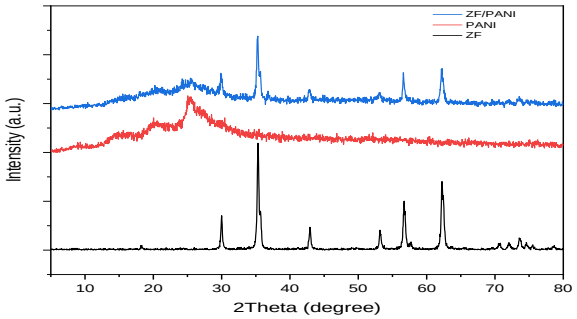

Fig.2. XRD patterns of $ZnFe_2O_4$ nanoparticles, PANI, and prepared nanocomposite.

Surface topology

The surface topography of ZnFe2O4 nanoparticles, PANI, and the prepared nanocomposite was studied by atomic force microscopy. Fig.3 the AFM image of ZnFe2O4 nanoparticles shows a Granular shape with a nearly uniform distribution of the particles, where the irregularity of the particles is due to the agglomeration of ZnFe2O4 nanoparticles. While the PANI and the nanocomposite are irregular in shape with a heterogeneous distribution, where increases in the nanocomposite as a result of the presence of ZnFe2O4 nanoparticles gathering on the surface of PANI [14]. Table.2 shows the surface roughness parameters of prepared nanocomposite. The positive Rsk value of prepared materials assigned to the distribution of peaks more than the valleys on the surface. Where the Rku value show two cases; spiky nature (Rku>3) shows in ZnFe2O3 AFM image, and bumpy nature ((Rku<3) shows PANI and

PANI composite [15, 16].

Table 2.Statistical roughness parameters of the prepared materials.

NO.	Prepared materials	Ra (nm)	Rsk	Rku
1	ZnFe2O4	39.876	1.917	5.677
2	PANI	134	0.666	2.527
3	ZnFe2O4/PANI	235	0.931	2.294

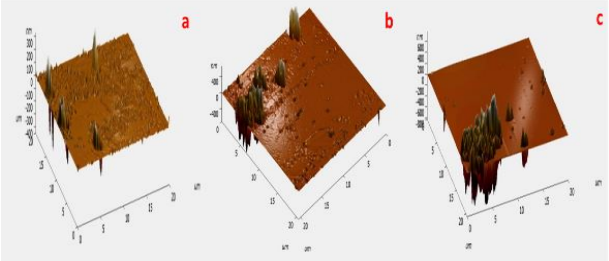

Fig.3.The AFM images of (a) $ZnFe_2O_4$, (b) PANI, and (c) prepared nanocomposite.

Surface morphology

The study of the mixing state of components, size, aggregation state of nanofiller, and morphology is a significant interest in the field of nanocomposites. As shown in Fig. 4, the surface morphology of nanocomposites was investigated using field emission scanning electron microscopy (FE-SEM). The spherical shape is shown in Fig. 4.(a) due to ZnFe2O4 nanoparticles, where nanoparticles are less than 100 nm in size and are dense and randomly scattered throughout the area. Additionally, tiny particle aggregation was found, Because nanomaterials have high surface energies, the presence of pore-free crystallites on the surface is owing to the agglomeration of tiny particles. In addition, the calcination process has a great effect on the aggregation of primary particles and it is also difficult to avoid this phenomenon due to the use of high temperatures (600 °C) to complete the process of growing ZnFe2O4 crystals. Zinc ferrite's average size range was found to be (65-75) nm [8]. While the pure PANI has a wires-like fiber network structure (nanorod) with a rough surface as shown in Fig. 4. (b). Fiber chains range in length from 200 to 500 nm [17].

The morphology of the produced nanocomposite is heavily controlled by the ratio of mixing components and the Preparation method. Fig. 4. (c-d) with low and high magnification showed the nanocomposite ZnFe2O4-PANI. Where ZnFe2O4 nanoparticles adhere to the wires network matrix surface without significantly affecting the polymer shape. The aggregated ZnFe2O4 nanoparticles are widely distributed throughout the polymer matrix in PANI. Because of the in situ oxidation polymerization of PANI using sonication, no aggregation of ZnFe2O4 nanoparticles is found and the average size range of zinc ferrite nanoparticles was been (30-50) nm. Additionally, the surface roughness has improved [18].

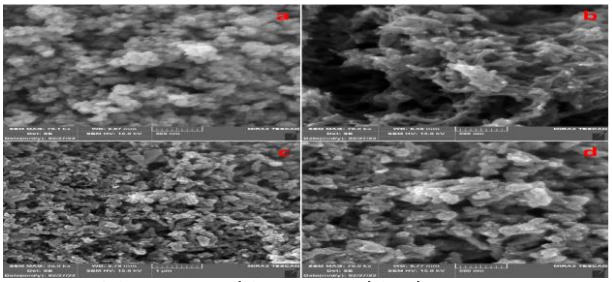

Fig. 4. (a) $ZnFe_2O_4$ (b) PANI and (c-d) ZnFe2O4-PANI nanocomposite.

Surface area and porosity

Fig.5 displays the nitrogen adsorption-desorption isotherms of synthesized nanocomposites obtained by the BET with the Pore size distribution determined by the BJH. The isotherms can be classified as type IV according to the classification proposed by the International Union of Pure and Applied Chemistry (IUPAC), which indicates monolayer adsorption followed by multilayer formation and capillary condensation to mesoporous nanocomposite [19].

The hysteresis loops can be studied by the pore configuration were described as Type H3 hysteresis loops which suggest narrow slit-shaped pores that are generally associated with sheet-like particles with non-rigid aggregates. This result complies with their morphology (Fig.4). The results obtained from the surface area Analysis (BET) are shown in Table 3, where the diameter of mesoporous materials was large than 2 nm, and dispersed, nonporous, or total pore volume of pores less was than 98.7808 nm. The results showed that nanocomposite can be classified as mesoporous based on the average pore diameter (13.18679 nm) [17].

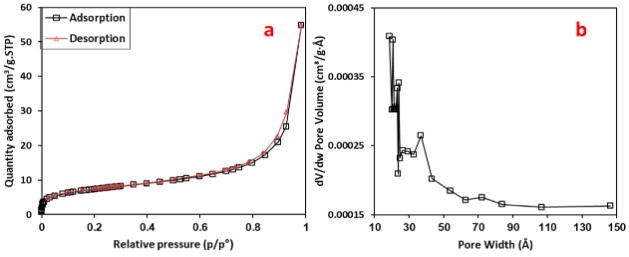

Fig. 5. (a) BET isotherms of Nitrogen adsorption-desorption of prepared nanocomposite (b) BJH pore size distribution curve.

Table 3. Isotherm type, hysteresis loop, surface area, pore volume, and average diameter of ZF-PANI nanocomposite.

prepared materials	Isotherm type	Hysteresis loop	Surface area (m^2/g^{-1})	Total pore Volume ($cm^3\ g^{-1}$)	average pore diameter (nm)
ZnFe2O4/PANI	4	H3	24.8534	0.081934	13.18679

Magnetic Analysis

The vibrating sample magnetometer (VSM) is a widely known technique for analyzing the magnetic nature of adsorbents. In a magnetic field at 1000 gauss, as shown in Fig. 6, the saturation magnetization of ZnFe2O4-PANI nanocomposite is 0.08059 emu g-1, which is lower than pure ZnFe2O4 nanoparticles in previous literature [10]. As a result, the sample's magnetization curve exhibits weak

ferromagnetic behavior with hysteresis. In addition, the saturation magnetization value of the ZnFe2O4-PANI nanocomposite was reduced due to the impregnation of a few percent of pure ZnFe2O4 in PANI [20], and the formation of the ZnFe2O4-PANI composite that was clearly in Fig. 7 for TGA images.

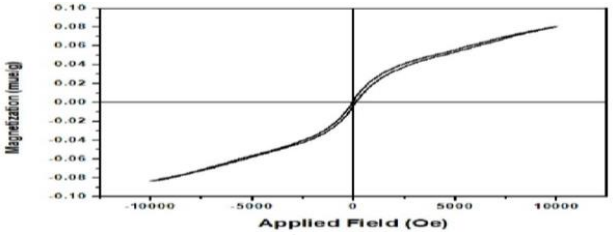

Fig 6. VSM analysis of prepared $ZnFe_2O_4$-PANI nanocomposite.

Thermal Analysis

The Thermogravimetric analysis results of ZnFe2O4 nanoparticles and ZnFe2O4-PANI nanocomposite are shown in Fig. 7. At temperatures ranging from 40 to 800 °C, the TGA curve of ZnFe2O4 nanoparticles reveals one step of weight loss due to moisture expulsion (physically adsorbed water), which indicates the formation of pure ZnFe2O4 nanoparticles [21]. While The TGA curve of the ZnFe2O4-PANI nanocomposite reveals two steps in weight loss; the first step indicates moisture expulsion in the temperature range of 40 to 150 °C. The breakdown of a volatile chemical link between the ZnFe2O4 nanoparticles and PANI in addition to the decomposition of the backbone PANI chain is responsible for the second step of weight loss in the temperature range of 220-650 °C [22].

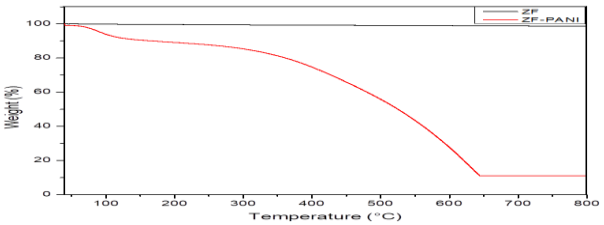

Fig 7. TGA curves of $ZnFe_2O_4$ nanoparticles and $ZnFe_2O_4$-PANI nanocomposite.

Effect of Contact Time and Adsorption Kinetics

The appropriate equilibrium time was studied to remove a certain concentration of the adsorbed dyes OG and MG by a superimposed surface at a temperature of 25°C and pH = 7 and constant weight of the composite 0.01g and at a concentration of 50ppm and 30ppm of both dyes OG and MG, respectively for different periods of time ranging (5-120) min. And through Fig. 8(a), the results showed that the time required to reach the equilibrium state for OG and MG dyes is 80 min, as the amount of adsorbed dyes increases significantly and rapidly during the first minutes of the adsorption process, after which the increase will be gradual until reaching to the time required for equilibrium, the reason for the rapid increase in the amount of adsorbed dyes is due to the presence of a large number of active centers at the beginning of the adsorption process that is unoccupied and sufficient for the adsorption of dyes . After that, the adsorption process become slow and more difficult due to the occupancy of all surface active centers with dye molecules [23].

The study of adsorption kinetics is important in determining the time period during which the adsorption process occurs as well as the extent of its impact on the efficiency of adsorption, as fixed concentrations of the two dyes and OG and MG were used at a concentration of 50 ppm and 30 ppm, respectively and a temperature of 25°C where the adsorption rate decreases or rises with time. To investigate the effect of the surface of the ZF-PANI adsorbent nanocomposite on the rate of adsorption, kinetic models were used to describe the experimental data, and the most common models followed by the adsorption process are the pseudo-first-order model and the pseudo-second-order model. The two models are being expressed as follows:

Model of pseudo-first-order (linear form)

$$\ln(q_e - q_t) = \ln q_e - k_1 t \quad (4)$$

Model of pseudo-second-order (linear form)

$$\frac{t}{q_t} = \frac{1}{k_2 q_e^2} + \frac{1}{q_e} t \quad (5)$$

Where qe and qt are the amounts of OG and MG adsorbed at equilibrium (mg /g) and at (t) time, k1 is the overall rate constant of pseudo-first-order kinetics (mg / (min.g)), and k2 is the pseudo-second-order rate constant (mg /(g. min)).

In the pseudo-first-order and pseudo-second-order models, as shown in Fig. 8(b) and (c) and by calculating the correlation coefficients and kinetic constants for both models shown in Table 4, the results showed that the value of the correlation coefficient (R2) is relatively high for the pseudo-second-order model compared to the pseudo-first-order model, and we conclude from this that the adsorption process of OG and MG dyes on the nanocomposite surface follows the pseudo-second-order mode [23, 24].

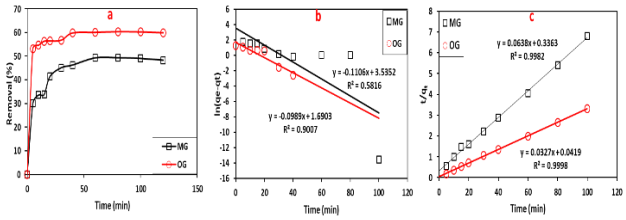

Fig. 8. The removal and kinetics graphs models: (a) the removal (b) pseudo-first-order and pseudo-second-order models of (c).

Table 4. Kinetic data of adsorption OG and MG on to ZF-PANI nanocomposite.

First order	Second order	First order	Second order	First order	Second order	First order	Second order
Dye	qeexp (mg/g)	k1 (min-1 mg g-1)	qe cal (mg/g)	R2	k2 (min. g/mg)	qe cal (mg/g)	R2
OG	30.1069	0.0989	5.4211	0.9007	0.0255	30.5810	0.9998
MG	14.7116	0.1106	34.302	0.5816	0.0121	15.6739	0.9982

Adsorbent dosage

Different weights were taken from the prepared composites ranging (0.005-0.05g), and at a concentration 50ppm of OG and 30ppm of MG dye, 10 ml of dye solution was added to the prepared weights at a temperature of 25°C where was observed that the adsorption increases

with the increase in the weight of the adsorbent material and the reason for this is due to the increase in the active groups through which adsorption occurs, where the adsorption process requires a balance between the adsorbent and the adsorbate in order for all the active centers of the adsorbate to be occupied and this in turn makes the adsorption process stable on the surface, and when all the active sites are connected to the adsorbate particles, the amount of the adsorbent will reach the highest value after that, the large increase in the weight of the adsorbent surface leads to an unstable spread of the adsorbent surface compared to the amount of the adsorbed material, and this leads to the overcoming of the dissolution energy of the adsorbent material over the adsorption energy of the surface, which in turn leads to a decrease in the amount of the adsorbent material on the surface [25, 26]. The maximum removal of MG dye was taken with the dosage (0.05g), as for the OG dye removal with the dosage (0.03 g), which was used for all subsequent experiments. Fig. 9. Shows the effects of different weights on the adsorption process.

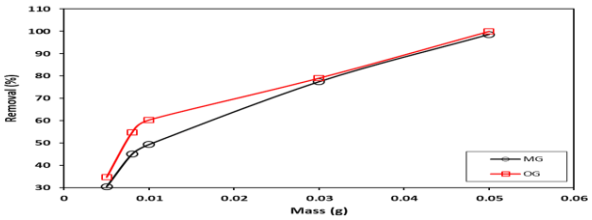

Fig. 9. Effect of adsorbent dosage on the adsorption process.

Adsorption isotherm studies

An isotherm study was conducted for the adsorption of OG and MG dyes on the surface of the composite at a temperature of 25°C, pH=7, and a concentration of 50ppm and 30ppm of both dyes OG and MG, respectively. Fig. 10(a) and (b) shows the analysis of the results of the adsorption process according to the classification of Giles, the results showed that the adsorption process of OG and MG dye corresponds to the L4 class or the so-called Langmuir type 4, in which the adsorption is single-layer and the orientation of the adsorbed molecules is horizontal on the adsorbent surface [27]. The Langmuir, Freundlich, and Timken isothermal equation models have been applied to describe the adsorption properties of the adsorbent, which are the most common as follows [28].

Model of Langmuir isotherm

$$\frac{C_e}{q_e} = \frac{C_e}{q_m} + \frac{1}{K_L q_m} \quad (6)$$

Model of Freundlich isotherm

$$\log q_e = \log K_f + {}^{1}/_{n}\,(\log C_e) \quad (7)$$

Model of Timken isotherm

$$q_e = B_1 \ln K_T + B_1 \ln C_e \quad (8)$$

Where qe =the amount of OG and MG adsorbed (mg/g) at Ce (equilibrium state), qm and kL are Langmuir constant related to maximum efficiency of adsorption and energy of adsorption, respectively. Kf and 1/n are Freundlich isotherm constant and intensity of adsorption, respectively. B1=RT/b, where (T) is the temperature (K) and (R) is the ideal gas constant (J/(mol. K)) while (b) indicates the Timken constant.

As shown in Table (5) and Fig. (11), the Langmuir isotherm shows a great match for the adsorption of OG and MG dyes in a better way compared to the two models of Freundlich and Timken, and this is shown by the value of the correlation coefficient (R2) which is equal to 0.9912 and 0.9982, respectively. That the compatibility of the Langmuir isotherm with the adsorption process data indicates the homogeneous nature of the adsorbing surface and that the active centers are of equivalent energy, and then a single molecular layer of the adsorbed dye is formed on the surface of the prepared nanocomposite [29].

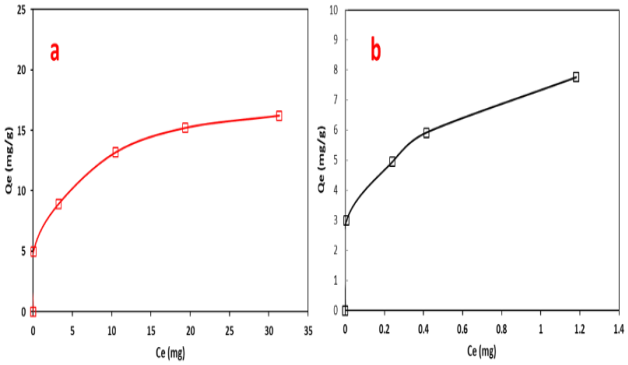

Fig 10. Adsorption isotherm (a) OG dye (b) MG dye.

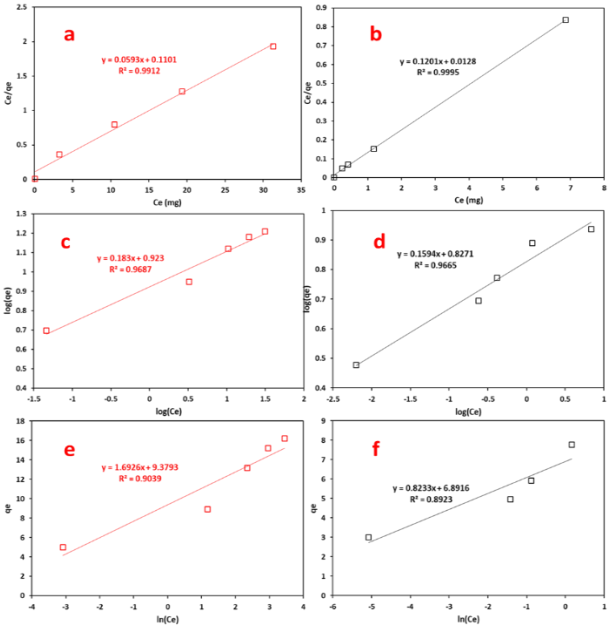

Fig. 11. Plot for adsorption (a,b) Langmuir model, (c,d) Freundlich model, and (e,f) Temkin model of OG and MG dyes, respectively at pH 7 and 25 °C.

Table 5. Shows data for isotherm models of OG and MG adsorption.

	Langmuir isotherm			Freundlich isotherm			Temkin isotherm		
	Ka (L.mg-1)	qm (mg/g)	R2	KF (mg/g (L/mg)1/n)	n	R2	KT (L.g-1)	B	R2
OG	0.5386	16.8634	0.9912	8.3753	5.4645	0.9687	255.0237	1.6926	0.9039
MG	9.2828	8.3264	0.9995	6.7158	6.2735	0.9665	4318.672	0.8233	0.8923

Initial pH effect

The effect of pH on the adsorption process of OG and MG

dyes on the surface of the adsorbent nanocomposite ZF-PANI at specific values of pH within the ranges (2, 6, 11) was studied with the stability of conditions such as temperature, equilibrium time, the concentration of each dye, and the weight of the adsorbent surface for each dye as shown in Fig. 12.

It is important to know the factors which affect the solution-adsorbent interface in understanding the adsorption phenomena. The solution pH is well-known as a substantial parameter in the adsorption phenomenon because it has a significant impact on the ionization state of adsorbate molecules in solution as well as the adsorbent`s surface properties [30]. Since the mixing ratio between PANI and ZF nanoparticles is (9:1), the point of zero charge (PZC) of PANI has significant effect on the composite (pH PZC=7.5) of PANI. As a result, the surface charge of the ZA-PANI will be positively charged when the pH is less than ZPC and negatively charged when the pH is more than ZPC [31]. The adsorption of OG dye increases at pH = 2 and then gradually decreases until it reaches pH = 10, and the reason for this is that the pKa values of the OG dye molecule are 1 and 11.5 for the deprotonation/ionization of the sulfate and hydroxyl group, respectively. Therefore, the OG dye is a highly negatively charged dye at an acidity greater than 1 and because the surface charge of the adsorbent is positive as a result of protonation in an acidic medium, an electrostatic attraction occurs between them. And the force of attraction decreases with a decrease in the concentration of H+ ions (increasing pH). At pH = 10, deprotonation of the nitrogen atoms of the polymer chain and competitive interaction between OH- ions and anions of the OG dye molecule present in the alkaline solution may cause a decrease in The adsorption of OG dye. While the absorption of MG dye gradually increases when the pH rises from 2.0 to 10.0, the reason is attributed to the decrease in the protonation process on the adsorbed surface and the appearance of the electron pair on the nitrogen atom, which leads to the occurrence of electrostatic attraction with the positive dye[31]. Nonetheless, the adsorption appeared good at all pH values, implying that electrostatic interactions were not the only type in the adsorption mechanism. Van der Waal forces, hydrogen bonding, and Hydrophobic-hydrophobic interaction are all prevalent [32].

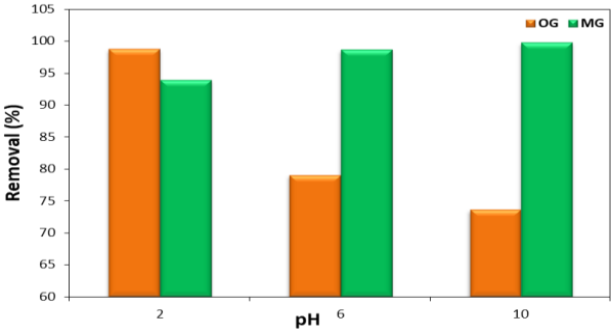

Fig. 12. The influence of pH on the adsorption of OG and MG dyes.

Thermodynamics

In this study, the values of thermodynamic functions were calculated in explaining the adsorption process of OG and MG dyes on the surface of the prepared composite. Since thermodynamic functions are important in understanding the adsorption process, as they give a good description of the nature of the regularity of the dye molecules resulting from molecular interactions by measuring the change in entropy ΔS°, Change of energy ΔG°, and by measuring the change in enthalpy ΔH°, it is possible to know the forces controlling it are they Chemical or physical, as well as knowing the direction of the reaction. Can be determined ΔG°, ΔS°, and, ΔH° from the following equations

$$\Delta G^\circ = -RT \ln K \quad (9)$$

$$\Delta G^\circ = \Delta H^\circ - T\Delta S^\circ \quad (10)$$

From equations (9) and (10), to get equation (11)

$$\ln K = \frac{\Delta S^\circ}{R} - \frac{\Delta H^\circ}{RT} \quad (11)$$

The intercept and slope of the linear plots were used to compute the values of (ΔS°/ R) and (-ΔH°/ R). In Fig.13 (a) OG dye and (b) MG dye. Table (6) shows the values of thermodynamic functions for the adsorption process of OG and MG dyes, where the negative value of free energy (ΔG°) indicated that the adsorption process was spontaneous. The negative value of the enthalpy (ΔH°) indicates that the OG and MG dye adsorption process is an exothermic process, which indicates that the mutual action between the adsorbate surface and the dye molecules will decrease With the increase in temperature, the reason for this is due to the separation and smashing of the bonds formed between the active centers of the adsorbate surface and the dye molecules [33, 34].

Table 6. The thermodynamic parameters of adsorption of OG and MG dyes on the ZF-PANI surface.

Dye	ΔH°(KJ.mol-1)	ΔG° (J.mol-1)	ΔS° (J.mol-1.K-1)
OG	-25217.2	-3289.1	-73.96
MG	-51335.6	-10578.5	-139.52

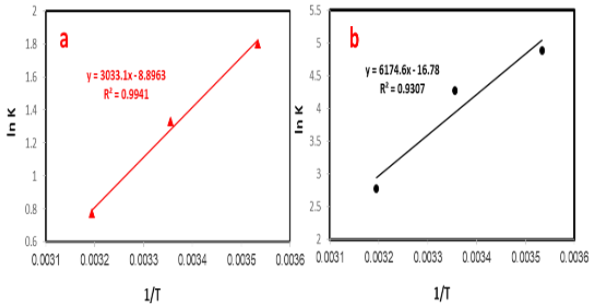

Fig 13. Van't Hoff plots for the adsorption of (a) OG dye and (b) MG dye onto the ZF-PANI surface.

4. Conclusion

In this research, ZnFe2O4 Nanoparticles were synthesized using a co-precipitation method and impregnating PANI onto ZnFe2O4 by in-situ polymerization under ultrasonic fields. XRD, FE-SEM, VSM, BET, BJH, FT-IR, AFM, and TGA were used to characterize the magnetic nanocomposite of (PANI-ZnFe2O4). The resultant composite was used to remove Orange G dye and malachite green dye from an aqueous solution. By increasing the amount of adsorption dosage, the adsorption rate increased considerably, while the removal efficiency of OG and MG reached a maximum at pH 2 and 10, respectively. The kinetic adsorption was

better discussed by the pseudo-second-order model for both two dyes. The adsorption behavior and the equilibrium data were represented by the Langmuir isotherm model. The thermodynamic study concluded that the OG and MG adsorption using ZnFe2O4-PANI composite were spontaneous in nature and exothermic.

References

1. Naz M, Rafiq A, Ikram M, Haider A, Ahmad SOA, Haider J, Naz S. Elimination of dyes by catalytic reduction in the absence of light: A review. Journal of Materials Science. 2021;56(28):15572-608. https://doi.org/10.1007/s10853-021-06279-1
2. Freitas TKFS, Almeida CA, Manholer DD, Geraldino HCL, Souza MTFd, Garcia JC. Review of utilization plant-based coagulants as alternatives to textile wastewater treatment. In: Detox Fashion. Springer, 2018. p. 27-79. https://doi.org/10.1007/978-981-10-4780-0_2
3. Chowdhury MF, Khandaker S, Sarker F, Islam A, Rahman MT, Awual MR. Current treatment technologies and mechanisms for removal of indigo carmine dyes from wastewater: A review. Journal of Molecular Liquids. 2020;318:114061. https://doi.org/10.1016/j.molliq.2020.114061
4. Errais E, Duplay J, Darragi F, M'Rabet I, Aubert A, Huber F, Morvan G. Efficient anionic dye adsorption on natural untreated clay: Kinetic study and thermodynamic parameters. Desalination. 2011;275(1-3):74-81. https://doi.org/10.1016/j.desal.2011.02.031
5. El-Geundi M, Ismail H, Attyia K. Activated clay as an adsorbent for cationic dyestuffs. Adsorption Science & Technology. 1995;12(2):109-17. https://doi.org/10.1177/026361749501200203
6. Patil MR, Shrivastava V. Adsorption of malachite green by polyaniline–nickel ferrite magnetic nanocomposite: an isotherm and kinetic study. Applied Nanoscience. 2015;5(7):809-16. https://doi.org/10.1007/s13204-014-0383-5s
7. Sambhudevan S. Ferrite-based polymer nanocomposites as shielding materials: a review. Chemical Papers. 2021;75(8):3697-710. https://doi.org/10.1007/s11696-021-01664-1
8. Khoso WA, Haleem N, Baig MA, Jamal Y. Synthesis, characterization and heavy metal removal efficiency of nickel ferrite nanoparticles (NFN's). Scientific Reports. 2021;11(1):1-10. https://doi.org/10.1038/s41598-021-83363-1
9. Singh G, Chandra S. Nano-flowered manganese doped ferrite@ PANI composite as energy storage electrode material for supercapacitors. Journal of Electroanalytical Chemistry. 2020;874:114491. https://doi.org/10.1016/j.jelechem.2020.114491
10. Vinosha PA, Mely LA, Jeronsia JE, Krishnan S, Das SJ. Synthesis and properties of spinel ZnFe2O4 nanoparticles by facile co-precipitation route. Optik. 2017;134:99-108. https://doi.org/10.1016/j.ijleo.2017.01.018
11. Feng J, Hou Y, Wang X, Quan W, Zhang J, Wang Y, Li L. In-depth study on adsorption and photocatalytic performance of novel reduced graphene oxide-ZnFe2O4-polyaniline composites. Journal of Alloys and Compounds. 2016;681:157-66. https://doi.org/10.1016/j.jallcom.2016.04.146
12. Mostafaei A, Zolriasatein A. Progress in natural science: materials international synthesis and characterization of conducting polyaniline nanocomposites containing ZnO nanorods. Prog Nat Sci Mater Int. 2012;22(4):273-80.
13. Chen SA, Lee HT. Polyaniline plasticized with 1-methyl-2-pyrrolidone: structure and doping behavior. Macromolecules. 1993;26(13):3254-61. https://doi.org/10.1021/ma00065a002
14. Ismail MM, Rafeeq SN, Sulaiman J, Mandal A. Electromagnetic interference shielding and microwave absorption properties of cobalt ferrite CoFe2O4/polyaniline composite. Applied Physics A. 2018;124(5):1-12. https://doi.org/10.1007/s00339-018-1808-x
15. Sharifi-Viand A, Mahjani MG, Jafarian M. Determination of fractal rough surface of polypyrrole film: AFM and electrochemical analysis. Synthetic metals. 2014;191:104-12. https://doi.org/10.1016/j.synthmet.2014.02.021
16. Tayebi N, Polycarpou AA. Modeling the effect of skewness and kurtosis on the static friction coefficient of rough surfaces. Tribology international. 2004;37(6):491-505. https://doi.org/10.1016/j.triboint.2003.11.010
17. Das P, Nisa S, Debnath A, Saha B. Enhanced adsorptive removal of toxic anionic dye by novel magnetic polymeric nanocomposite: optimization of process parameters. Journal of Dispersion Science and Technology. 2022;43(6):880-95. https://doi.org/10.1080/01932691.2020.1845958
18. Ghadimi LS, Arsalani N, Tabrizi AG, Mohammadi A, Ahadzadeh I. Novel nanocomposite of MnFe2O4 and nitrogen-doped carbon from polyaniline carbonization as electrode material for symmetric ultra-stable supercapacitor. Electrochimica Acta. 2018;282:116-27. https://doi.org/10.1016/j.electacta.2018.05.160
19. Desai HB, Hathiya LJ, Joshi HH, Tanna AR. Synthesis and characterization of photocatalytic MnFe2O4 nanoparticles. Materials Today: Proceedings. 2020;21:1905-10. https://doi.org/10.1016/j.matpr.2020.01.248
20. Mohammadi H, Ghaedi M, Fazeli M, Sabzehmeidani MM. Removal of hexavalent chromium ions and acid red 18 by superparamagnetic CoFe2O4/polyaniline nanocomposites under external ultrasonic fields. Microporous and Mesoporous Materials. 2021;324:111275. https://doi.org/10.1016/j.micromeso.2021.111275
21. Khairy M. Synthesis, characterization, magnetic and electrical properties of polyaniline/NiFe2O4 nanocomposite. Synthetic metals. 2014;189:34-41. https://doi.org/10.1016/j.synthmet.2013.12.022
22. Wang C, Shen Y, Wang X, Zhang H, Xie A. Synthesis of novel NiZn-ferrite/Polyaniline nanocomposites and their microwave absorption properties. Materials science in semiconductor processing. 2013;16(1):77-82. https://doi.org/10.1016/j.mssp.2012.06.015

23. Bhattacharyya R, Ray SK. Removal of congo red and methyl violet from water using nano clay filled composite hydrogels of poly acrylic acid and polyethylene glycol. Chemical Engineering Journal. 2015;260:269-83. https://doi.org/10.1016/j.cej.2014.08.030
24. Waheeb AS, Alshamsi HAH, Al-Hussainawy MK, Saud HR. Myristica fragrans shells as potential low cost bio-adsorbent for the efficient removal of rose Bengal from aqueous solution: Characteristic and kinetic study. Indonesian Journal of Chemistry. 2020;20(5):1152-62. https://doi.org/10.22146/ijc.50330
25. Heidarizad M, Şengör SS. Synthesis of graphene oxide/magnesium oxide nanocomposites with high-rate adsorption of methylene blue. Journal of Molecular Liquids. 2016;224:607-17. https://doi.org/10.1016/j.molliq.2016.09.049
26. Mutar HR, Jasim KK. Adsorption study of disperse yellow dye on nanocellulose surface. Materials Today: Proceedings. 2021. https://doi.org/10.1016/j.matpr.2021.04.003
27. van der Stap J, Klaasse S. Labwaarden: Acute nierinsuffi ciëntie. Nursing. 2016;22(6):36-8. https://doi.org/10.1007/s41193-016-0111-5
28. Muhammad A, Shah A-u-HA, Bilal S, Rahman G. Basic Blue dye adsorption from water using Polyaniline/Magnetite (Fe3O4) composites: Kinetic and thermodynamic aspects. Materials. 2019;12(11):1764. https://doi.org/10.3390/ma12111764
29. Kulkarni MR, Revanth T, Acharya A, Bhat P. Removal of Crystal Violet dye from aqueous solution using water hyacinth: Equilibrium, kinetics and thermodynamics study. Resource-Efficient Technologies. 2017;3(1):71-7. https://doi.org/10.1016/j.reffit.2017.01.009
30. Yu H, Pang J, Ai T, Liu L. Biosorption of Cu2+, Co2+ and Ni2+ from aqueous solution by modified corn silk: Equilibrium, kinetics, and thermodynamic studies. Journal of the Taiwan Institute of Chemical Engineers. 2016;62:21-30. https://doi.org/10.1016/j.jtice.2016.01.026
31. Dlamini ML, Bhaumik M, Pillay K, Maity A. Polyaniline nanofibers, a nanostructured conducting polymer for the remediation of Methyl orange dye from aqueous solutions in fixed-bed column studies. Heliyon. 2021;7(10):e08180. https://doi.org/10.1016/j.heliyon.2021.e08180
32. Ahmad R, Kumar R. Conducting polyaniline/iron oxide composite: a novel adsorbent for the removal of amido black 10B. Journal of Chemical & Engineering Data. 2010;55(9):3489-93. https://doi.org/10.1021/je1001686
33. Katal R, Pourkarimi S, Bahmani E, Dehkordi HA, Ghayyem MA, Esfandian H. Synthesis of Fe3O4/polyaniline nanocomposite and its application for nitrate removal from aqueous solutions. Journal of Vinyl and Additive Technology. 2013;19(2):147-56. https://doi.org/10.1002/vnl.21306
34. Taheri FS, Ghaemi A, Maleki A, Shahhosseini S. High CO2 adsorption on amine-functionalized improved mesoporous silica nanotube as an eco-friendly nanocomposite. Energy & Fuels. 2019;33(6):5384-97. https://doi.org/10.1021/acs.energyfuels.9b00703